Journal of Applied Physics

RESEARCH ARTICLE | DECEMBER 08 2023

Large-volume CdZnTe bar detectors characterized by laser-induced transient currents

M. Betušiak ; P. Praus ; R. Grill ; E. Belas ; J. Pipek ; A. E. Bolotnikov ; R. B. James

J. Appl. Phys. 134, 224501 (2023)
https://doi.org/10.1063/5.0160766

Journal of Applied Physics ARTICLE pubs.aip.org/aip/jap

Large-volume CdZnTe bar detectors characterized by laser-induced transient currents

Cite as: J. Appl. Phys. **134**, 224501 (2023); doi: 10.1063/5.0160766
Submitted: 31 July 2023 · Accepted: 14 November 2023 ·
Published Online: 8 December 2023

M. Betušiak,[1,a)] P. Praus,[1] R. Grill,[1] E. Belas,[1] J. Pipek,[1] A. E. Bolotnikov,[2] and R. B. James[3]

AFFILIATIONS

[1]Charles University, Faculty of Mathematics and Physics, Institute of Physics, Ke Karlovu 5, Prague 2, CZ-121 16, Czech Republic
[2]Brookhaven National Laboratory, Upton, New York 11973, USA
[3]Savannah River National Laboratory, Aiken, South Carolina 20808, USA

[a)]**Author to whom correspondence should be addressed:** majo.betusiak@gmail.com

ABSTRACT

In this work, we studied the free-carrier transport properties and space-charge formation/polarization in a CdZnTe bar-shaped radiation detector using the Laser-Induced Transient Current technique. We found out that a steady-state space charge ranging from 8×10^8 to 2.1×10^9 cm^{-3} is formed throughout the detector at about 0.5 s following biasing. The measured current waveforms were modeled by Monte Carlo simulations after taking into account the electric and weighting fields inside the detector and shielding box. Modeling of the unpolarized waveforms revealed an exceptionally high electron mobility-lifetime product $\mu_e\tau_e \geq 0.095$ cm^2 V^{-1}. The observed formation of positive space charge in the biased detector and linear scaling of the current waveform shapes on applied bias revealed that the detector polarization is attributed to carrier injection at the anode. Measurements in pulsed and DC bias in modified electrode geometry proved the surface-charge formation.

I. INTRODUCTION

Large-volume CdZnTe (CZT) gamma-ray detectors can achieve excellent energy resolution approaching the statistical limits when high-quality crystals with a low content of defects are used.[1,2] The production of such crystals is expensive principally due to the low yields. In order to reduce the high cost of large-volume high-quality CZT material, arrays of small cross sections (around 5×5 mm^2) were introduced[1] in the form of 15–30 mm long bar detectors with a high aspect ratio. Such crystals can be produced less expensively and with considerably higher yields. The geometry of such crystals is convenient for their assembly into arrays of virtual Frisch–grid detectors, which have been under development for several years.[3]

Over the years, large-volume detectors prepared from various materials (HPGe,[4,5] CdZnTe,[6,7] TlBr,[8,9] $CsPbBr_3$,[10] etc.) with different electrode configurations were studied (e.g., coplanar grid,[7,11] strip,[12,13] and Frisch grids[2,14]). The performance of such devices was mostly characterized by x-ray and gamma spectroscopy measurements with evaluations of the mobility-lifetime product by the Hecht equation fit.[15] The deviation of the collected charge from the theoretical prediction was often attributed to a space-charge formation in the biased detector (i.e., detector polarization[16,17]). The electric field profiles throughout the detector may be determined by studying the transient charge pulses for individual events. For a more detailed characterization of polarization phenomena and the electric field distortion, techniques based on the Pockels effect[6,14] have been used, which allow direct determination of the electric field. Gamma and x-ray scanning[5,18] and 3D-position sensing[14] were also used to study the response homogeneity. The use of pulse shape analysis (current transients[11]) offers the possibility to simultaneously determine the electric field and the charge carrier transport properties, although it was rarely reported in the literature.[11,19]

Prior investigations demonstrated that defects, such as tellurium inclusions and dislocations in CdZnTe detectors become increasingly problematic as the detector size increases.[18] Unfavorable effects of these defects can be suppressed to some extent by 3D mapping of charge-trapping inhomogeneities and incorporation of charge-loss corrections.[14] This way, it is possible to fabricate a high energy-resolution detector even from lower-quality crystals. Despite these corrections, the presence of a space charge that distorts the

internal electric field and subsequent formation of an inactive region are critical factors limiting the maximum detector size. This was proven in Ref. 14, where 3D corrections of ^{137}Cs spectra led to a FWHM of 0.76%, 1.06%, 1.10%, and 1.6% for 20, 30, 40, and 50 mm long bars, respectively. The authors of this paper reported that one of the reasons for the decreased energy resolution for the 50 mm detector is a lower electric field in a portion of the detector. Considering that large-volume detectors are particularly useful for high-energy gamma and hard x-ray detection, it is important to prevent or suppress the formation of either an inactive or low charge-transport layer. Usually, this can be achieved by applying a higher bias; however, tens of kV may be required for these types of thick detectors, which is impractical.

Here, we investigate the electron transport and space-charge formation in a bar detector with dimensions of $19.4 \times 6 \times 6\ \text{mm}^3$ using the laser-induced transient current technique (L-TCT).[20–23] In this work, we tested just one detector to demonstrate our approach and its benefits for characterizing CZT detectors for practical applications. Our priority is to identify the space-charge formation mechanism, which can help resolve the problem with a low electric-field region and allow the production of better-performing detectors. We also address unusual features observed in the charge-carrier dynamics and report models explaining their origins.

II. EXPERIMENTAL

A. Laser-induced transient current technique

The laser-induced transient current technique is based on recording and analyzing the shape of photoinduced current pulses.[20,22,24] As an L-TCT probe, we used 670 nm (1.85 eV) laser pulses (~500-ps long) generated by a SuperK Compact laser with a white spectrum. The laser pulse intensity was chosen small enough to avoid distortions of the applied electric field caused by the magnitude of drifting charge. The photogenerated charge was in the range of hundreds of fC, which corresponds to an energy of about 9 pJ/pulse (depending on the contact thickness, surface reflection, and recombination). Due to the low signal-to-noise ratio, ~10 thousand transients were averaged into a single current waveform. In Fig. 1, we introduce the coordinate system fixed with the sample. The center of the cathode (x = 0, y = 0, z = 0 mm) was illuminated with a roughly 0.2 mm^2 laser spot. The laser pulse spot is displayed in red in Fig. 1. Figure 1 also shows larger electrodes (green) added to make the electric field inside the detectors more uniform and modify the weighting field of the collecting electrode. Their effect is discussed in the last part of this manuscript.

Our experimental setup can bias the detector up to ±600 V in the pulsed and ±2 kV in DC regimes. The bias pulsing was used to control the space-charge formation in the sample. Moreover, a laser-pulse delay (relative to the bias pulse) was used to study the dynamic of the space-charge formation. Its timing diagram is illustrated in Fig. 2. Individual pulsing conditions are defined by the bias pulse width (150 μs–5 s or DC), depolarization time (100 ms–10 s), and laser-pulse delay (100 μs–5 s). There is no depolarization interval in the DC regime, so we use the laser pulsing period (10 ms) instead. A more detailed description of our setup can be found in Refs. 20, 21, and 23.

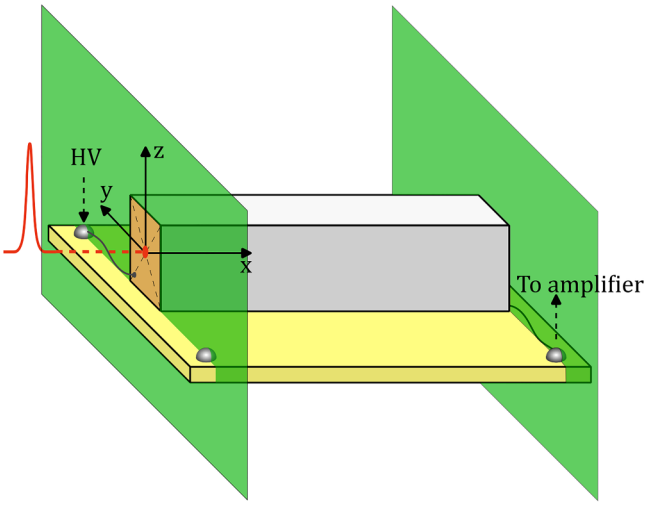

FIG. 1. Schematic of the experimental setup and illumination conditions. The additional electrodes used for making the uniform electric field are shown in green.

B. Detector description

In this paper, we studied a $Cd_{0.9}Zn_{0.1}Te$ detector with dimensions of $19.4 \times 6 \times 6\ \text{mm}^3$ grown by the traveling heater method (THM). It was acquired from Redlen Technologies, Inc. The detector material is slightly n-type, having a resistivity of $2 \times 10^{10}\ \Omega\,\text{cm}$ determined by I–V measurement. The detector was equipped with semi-transparent gold planar electrical contacts on both sides to allow photoexcitation of the sample.

III. THEORETICAL

According to the Shockley–Ramo theorem, the induced current waveform (CWF) is proportional to the product of the electric field and the weighting field of the collecting electrode. The measured current response is described by formula (1), where $Q(t)$ is the drifting charge and $\boldsymbol{v}(\boldsymbol{r})$ and $\boldsymbol{W}(\boldsymbol{r})$ are the drift velocity and the weighting field of the collecting electrode (i.e., detector's anode), respectively,[25]

$$I(t) = Q(t)\boldsymbol{v}(\boldsymbol{r}(t)) \cdot \boldsymbol{W}(\boldsymbol{r}(t)). \tag{1}$$

In planar samples, the weighting field is constant and is perpendicular to both electrodes, which allows for relatively easy determination of the electric field from the shape of the CWF. In a nonplanar geometry, the induced current calculations are more complex and require a three-dimensional approach due to the vector nature of electric and weighting fields and their spatial dependence.

For the determination of the electric field, we start with the weighting potential $\Phi_W(\boldsymbol{r})$ for which we can write

$$\frac{\partial \Phi_W(\boldsymbol{r}(t))}{\partial t} = \boldsymbol{W}(t) \cdot \frac{\partial \boldsymbol{r}(t)}{\partial t} = \boldsymbol{v}(t) \cdot \boldsymbol{W}(t). \tag{2}$$

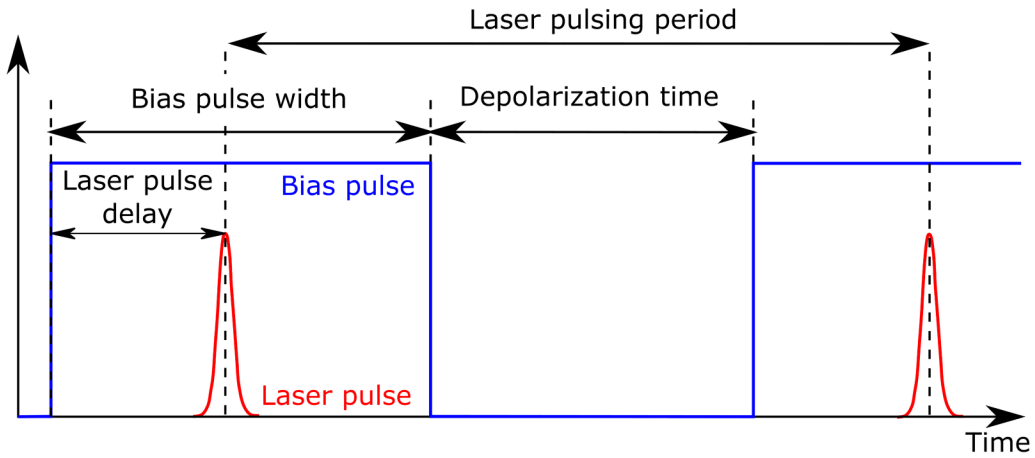

FIG. 2. Timing diagram of the laser and bias pulses.

From here, we relate the measured current $I(t)$ to the weighting potential of the collecting electrode $\Phi_I(t)$,

$$\int_0^t \frac{I(t')}{Q(t')}dt' = \Phi_I(t). \tag{3}$$

The evaluation of $\boldsymbol{v}(t)$ (and related electric field) is now only a matter of finding the correct function $\boldsymbol{r}(t)$ that ties $\Phi_I(t)$ and $\Phi_W(\boldsymbol{r})$ together. Because $\Phi_I(t)$ defines the equipotential surface on which electrons reside at time t, we also need to know the CWFs captured simultaneously from multiple electrodes (3D position sensing). Here, we applied a simpler approach based on a quasi-1D model, where the electron path follows one fixed field line calculated for an unpolarized detector or surface of the sample, if the field line exits the detector. In such a model, a single CWF contains all information needed to determine the position s along the chosen field line $\boldsymbol{r}(s)$. Provided the weighting potential along the chosen field line is uniquely defined by the position s, then $\Phi_I(t)$ can be substituted into the inverse function $s(\Phi_W)$. It is important to note that this simple model may be used only when the diffusion contribution to the current transient can be neglected, and the variation of the electric and weighting fields within the drifting charge region is negligible [i.e., a point-like charge $Q(t)$ is assumed]. The downside of the quasi-1D approach is that the assumed electron trajectory may deviate from the real one, which, in turn, affects the expected weighting field. Such drawbacks must be considered during the data interpretation. With assumptions that the charge trajectory along the bar-like sample remains fixed and matches the modeled trajectory, the electron lifetime τ_e is not affected by polarization and remains constant in the whole detector, and $Q(t)$ is given by $Q(t) = Q_0 e^{-t/\tau_e}$; then, we can obtain the electric field profile along the drift trajectory. Here, Q_0 is the initial photogenerated charge determined as the collected charge at the maximum bias. Considering that the weighting potential at the collecting electrode $\Phi_I(t_{tr})$ is by definition equal to 1 as it is prescribed by the Shockley–Ramo theorem,[25] the value of Q_0 is simply given by $Q_0 = \int_0^{t_{tr}} I(t')e^{t'/\tau_e}dt'$, where t_{tr} is the transit time. Note that the correctness of the evaluated electric field can be easily verified, since the line integral of the electric field along any field line between the cathode and ending at the anode must be equal to the applied bias.

IV. MODELING OF THE WEIGHTING FIELD

The electric and weighting fields were calculated using the Comsol Multiphysics software assuming the device geometry shown in Fig. 3. The detector (gray) is glued to the dielectric sample holder (yellow). For the calculation, values of the relative permittivity of the CZT $\varepsilon_{CdZnTe} = 10.9$ (Ref. 26) and the sample holder $\varepsilon_{holder} = 5.26$ were used. The ε_{holder} was determined by the capacitance measurement of a parallel-plate capacitor containing the sample holder. There are four conductive pads with attached pins in each corner of the sample holder. Two of them (see Fig. 1) are connected by 50 μm silver wires and silver paint to the detector electrodes, voltage source, and amplifier/ground. The remaining two pins are at a floating potential. The green board in the pictures of Fig. 3 represents the printed circuit board (PCB) used for readout. No conductive paths or electronic parts connected to or on this PCB were considered in the calculation, since the PCB is relatively far from the sample, and its components are small enough not to significantly affect the electric field. Conductive pads and pins on the sample holder, however, must be considered as they are close to the sample. Lastly, the detector and readout electronics are fully enclosed in the double ferromagnetic shield (gray and orange box). According to our calculations, this shielding is responsible for most of the field deformation besides the geometry of the detector itself. The ferromagnetic shielding and detector's collecting electrode are always grounded. The high voltage is applied only to the TCT-probed electrode of the detector.

Due to the large size of the simulated volume, we chose two different tetrahedral meshes for the computation of the weighting fields. In the proximity of the sample, 5–100 μm tetrahedral cells

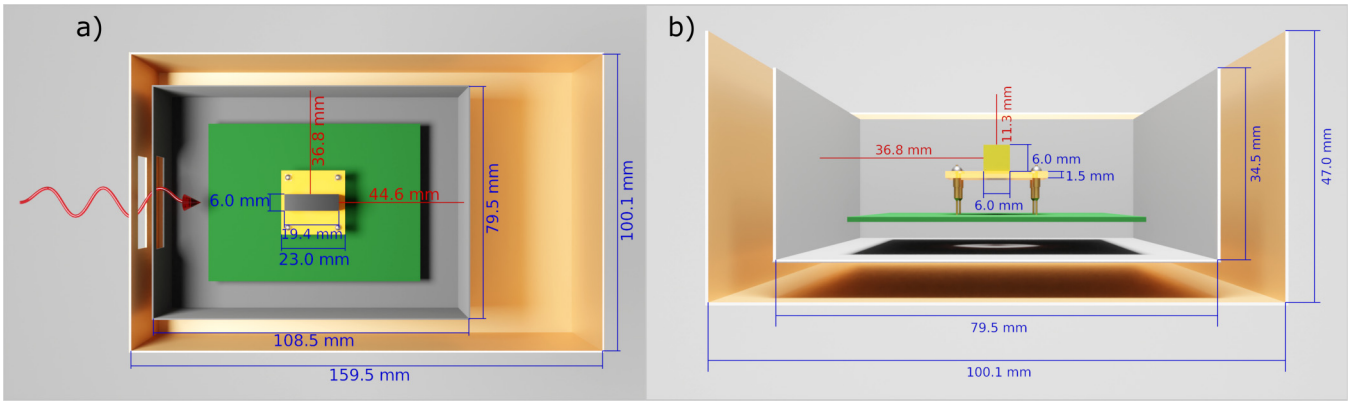

FIG. 3. (a) Top and (b) front views of the detector and our L-TCT setup. The dimensions used for the calculation of the electric and weighting fields are shown. Here, detector—gray (top view) and gold (front view), sample holder—yellow, conductive pads and pins—golden, readout PCB—green, and double ferromagnetic shielding—gray and orange. The dimensions displayed in red show the distance from the detector to the shielding.

were used, and 0.8–11.2 mm cells were used in the rest of the volume. The weighting potentials for the electrodes of interest were calculated by placing the chosen electrode at unit potential, while grounding the remaining electrodes (conductive parts of the setup) apart from the floating electrodes.

V. RESULTS AND DISCUSSION

A. Detector characterization

We first measured the current waveforms in an unpolarized detector to determine the lifetime and mobility of charge carriers. An unpolarized regime was attained by studying the detector immediately after biasing (100 μs), when no significant space charge was present. Keep in mind that because the cathode is located at x = 0 mm, all CWFs and electric fields are negative. In order to adhere to the CWF plotting convention, we plot the CWFs with the inverted current axis. Selected electron current transients are shown in Fig. 4(a). Their shape deviates from the flat or exponential profiles observed in planar detectors.[21,22,24,27] This distortion is caused by the inhomogeneous electric field and the weighting field representing the geometry of the sample and setup. In order to model the shape of the CWFs and to precisely evaluate the material's electrical transport parameters (lifetime and mobility), it was necessary to determine the electric

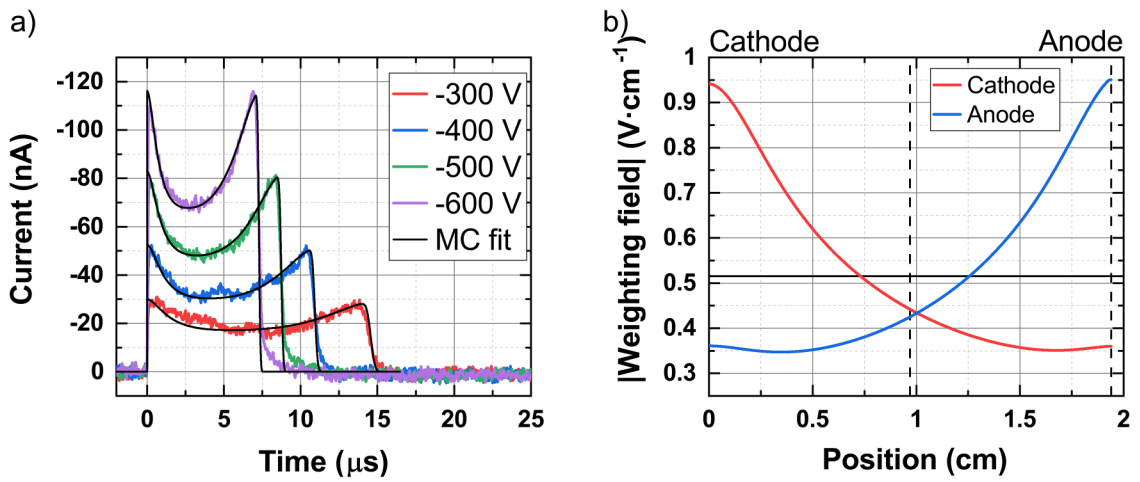

FIG. 4. (a) Bias dependence of selected electron current waveforms in an unpolarized sample and fits using Monte Carlo simulations. (b) Comparison of the absolute value of the weighting fields for the detector's cathode (positive) and anode (negative) for the bar detector in ferromagnetic shielding. The weighting fields are evaluated along the electric field line starting at the center of the cathode (x = 0, y = 0, z = 0 mm). The dashed lines show the position of the anode at 1.94 cm and the middle of the sample at 0.97 cm. The solid horizontal line represents the weighting field of a planar detector with the same thickness.

field inside the detector and the weighting field of the collecting electrode.[25]

The calculated electric and weighting fields along the field lines starting in the center of the cathode (x = 0, y = 0, z = 0 mm), as shown in Fig. 4(b), were included in the Monte Carlo (MC) simulation code.[19] The plots in Fig. 4(b) already represent the scalar product of the respective weighting fields and the unit vector tangent to the field line. Because the anode and the ferromagnetic shield are grounded, the electric field in the unpolarized detector is proportional to the applied bias and the cathode weighting field. The current waveforms are induced at all electrodes, but the signal is read out from the detector anode only. At first, most of the charge is induced at the cathode and the shielding. As the electrons move further toward the anode, the anode signal increases while the cathode signal decreases. At x = 9.7 mm, the positive charge induced in the shielding is at its maximum. Here, the electron cloud is the furthest from both the anode and the cathode. Because of this, the induced current at the ferromagnetic shielding switches its polarity.

The best fits shown in Fig. 4(a) were obtained when all immediate surroundings of the detector (i.e., ferromagnetic shielding, dielectric sample holder, electric contacts on the sample holder, and connecting wires) were included in the field calculations. Using the MC, we evaluated the electron mobility $\mu_e = 950\,\mathrm{cm^2\,V^{-1}\,s^{-1}}$ and lifetime $\tau_e \geq 100\,\mu\mathrm{s}$ indicating an excellent electron mobility-lifetime product $\mu_e\tau_e \geq 0.095\,\mathrm{cm^2\,V^{-1}}$. Unfortunately, the hole signal consisted of only exponentially decaying CWFs (not shown in this paper) with no apparent transit time (falling edge of CWF). The corresponding hole lifetime was $\tau_h \sim 5\,\mu\mathrm{s}$, while the hole mobility could not be accurately determined.

In the next step, we studied the space-charge formation in the biased detector. In this measurement, the detector was probed at various dwell times after applying a −600 V bias. The gradual changes of the electron transients due to the space-charge build-up are shown in Fig. 5(a). Apart from the amplitude, the CWF measured at 100 μs is the same as the CWF for −600 V in Fig. 4(a). CWFs remain stable during the first 20 ms corresponding to the unpolarized state of the detector, and then significant changes occur after ∼50 ms. The electric field in Fig. 5(b) was evaluated using the procedure described previously in the theoretical section. All the required criteria for the electric-field evaluation are met as the relative variation of the electric/weighting field over the illuminated spot is less than 0.2%, the diffusion broadening (∼50 μm) is negligible, and the electron lifetime is long enough not to affect the charge collection. Also, the weighting field varies within 10% in each *y*-*z* cross section of the sample. The error of the evaluated electric field due to an electron trajectory shift is therefore estimated to be within 10%.

The gradual increase in the transient current at t = 0 s and the electric field strength beneath the cathode proves the presence of positive space-charge formation in the bar. Applying Gauss law to the electric field profile in Fig. 5(b), we estimate the average space-charge density to be $\sim 8 \times 10^8\,\mathrm{cm^{-3}}$ in the steady state at 5 min after application of −600 V DC bias, when the space charge stopped forming. A similar electric field profile was observed by the Pockels effect in 5 cm-long bar detectors in Ref. 14. For the sake of the polarization model definition, it is also important to note that despite the polarization manifested by the significant transit time extension from 7.3 μs observed shortly after biasing to 13.3 μs at DC, the transit time is still observable. This means that the process of detector polarization terminates when the electric field strength near the anode diminishes to a low, but effectively nonzero value. Note that because we know the electric field only along one field line, the mentioned value also encompasses the effective contribution of space charge outside the electron trajectory.

It is also worth mentioning that the CWFs measured under a DC bias scale linearly over a wide interval of voltages (DC −0.6 to −1.8 kV), as shown in Fig. 6(a). To highlight this voltage

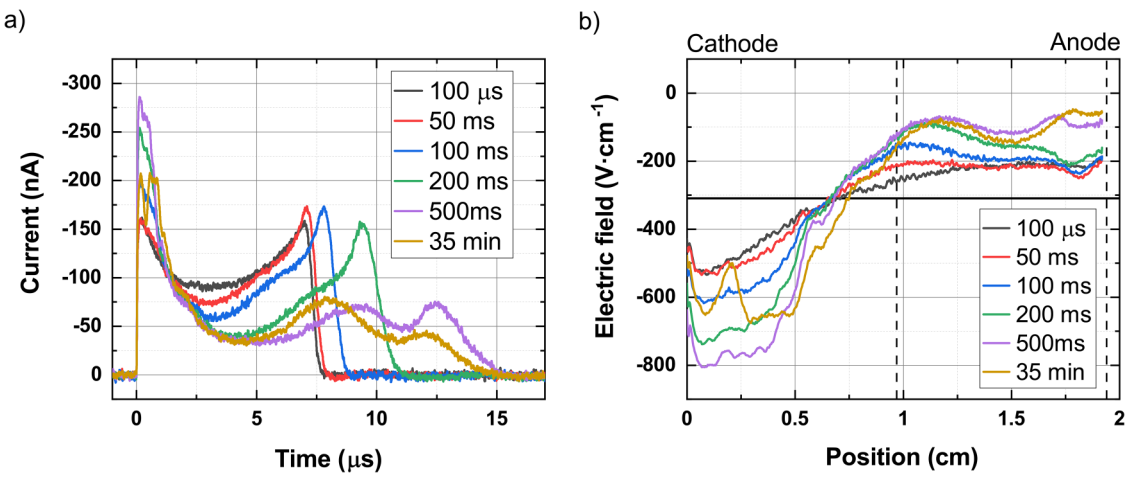

FIG. 5. (a) Changes of electron current transients after −600 V biasing. (b) The electric field evaluated from the current waveforms in (a). The solid horizontal line represents the electric field in the planar sample. The dashed vertical lines mark the middle (0.97 cm) and anode (1.94 cm) positions of the detector.

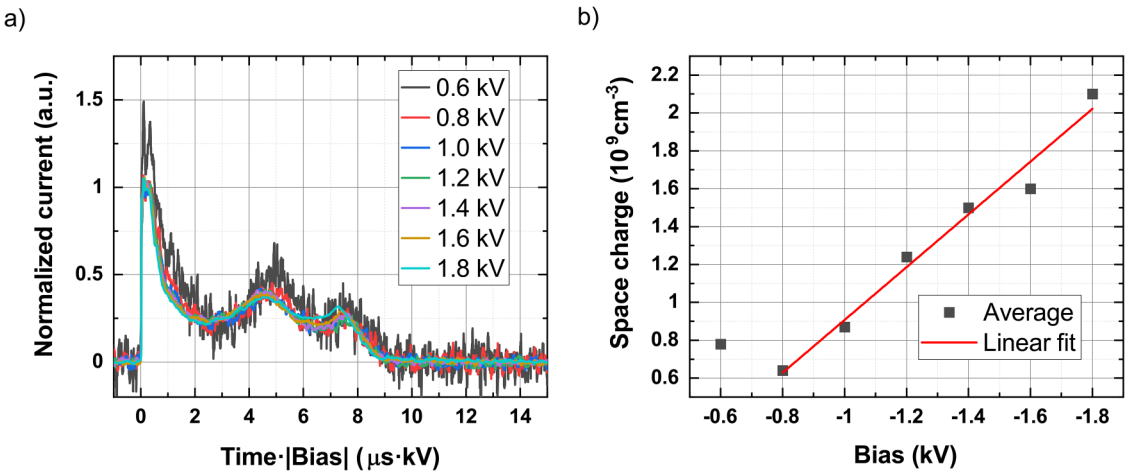

FIG. 6. (a) Normalized electron waveforms obtained 5 min after DC biasing. (b) Dependence of the average space-charge density on the applied bias. The charge density was determined using the 1D Gauss law from the electric field.

dependence, we plot CWFs against a bias-normalized time scale to compress CWFs measured at different biases to a similar time range and to better highlight the space-charge effect.[20] The similarity of the scaled CWFs is clearly seen after such normalization. In an unpolarized detector, this normalization aligns the falling edges of the current waveforms for all biases. In a polarized detector, the alignment strongly depends on the bias–space-charge relationship. Here, the bias normalization of the time scale results in the lining-up of whole steady-state CWFs. This leads to an important conclusion: the space charge responsible for deformation of the electric field varies linearly with the applied bias, as shown in Fig. 6(b).

Based on our findings, we consider the following models for polarization of the bar-type detector. There are two possible mechanisms responsible for positive space-charge formation—electron depletion or hole injection. The case of electron depletion due to a blocking cathode leads to a fixed space charge induced by the stabilization of the quasi-Fermi energy defined by the Schottky barrier at the cathode. In this case, the space charge spreads through the detector's bulk according to the well-known square root dependence[28] on the bias. This model does not produce linearly bias-dependent space charge and cannot explain the observed results. The injecting anode model offers a much more promising explanation. Because of hole injection, the electric field strength beneath the anode remains permanently low. Once the field strength near the anode increases/decreases, the electric current follows the trend in the same way, inducing a corresponding increase/decrease in the space charge, which damps respective deviations. Consequently, since the electric field strength near the anode is low, it fixes the total space charge necessary to screen the electric field appropriately (linearly), scaling the positive space charge at the cathode. This setting remains valid at each bias (in the studied polarity) unless the injecting ability of the anode declines. According to the proposed model, the space charge scales linearly with bias exactly as determined by the experimental observation. We thus conclude that we have unambiguously proven that the polarization of the detector is caused by hole injection from the anode.

The reasons for the bump in the central part of the CWFs formed at time >100 ms after biasing [see Fig. 5(a)] and the corresponding oscillation of the electric field near 1.5 cm [see Fig. 5(b)] are not yet satisfactorily explained. To better resolve these observations, we scanned the cathode (10×10 grid) and measured the transit time of the individual electron current waveforms for a DC bias of -600 V. The map of the resultant transit time is presented in Fig. 7(a). It clearly shows that the electron transit time is systematically higher near the left side of the sample (positive y). The central bump of the CWF is also more prominent in this region than in the region with a short transit time ($t_r < 12\,\mu$s). In addition, the total collected charge is nearly the same throughout the map, which proves that electrons reach the anode at all regions. In accordance with this recognition, the bump and longer transit time are consistent with electrons passing through the negative and positive space-charge region located primarily in the left side of the detector (positive y). The simultaneous formation of both positive and negative space charges in the bulk is not commonly observed in polarized detectors. We analyzed similar behavior in a semi-insulating GaAs:Cr detector, where we explained the effect by the presence of spatially variable hole conductivity.[20] Positive and negative space charges formed in this model also scale linearly with bias.

Alternative models depicting the bump formation are less convincing. Specifically, the bump could be an effect of variable effective electron mobility (shallow level trapping) or variable drift mobility (ionized impurity scattering). However, this model is not plausible. The bump is not present in the unpolarized detector, which means that the variation of the effective mobility cannot be caused by inhomogeneous shallow-level trapping. Space charge populates only the deep defect levels near the Fermi level. The highest estimated space-charge density 2.1×10^9 cm^{-3} is also much lower than the characteristic ionized impurity density that could

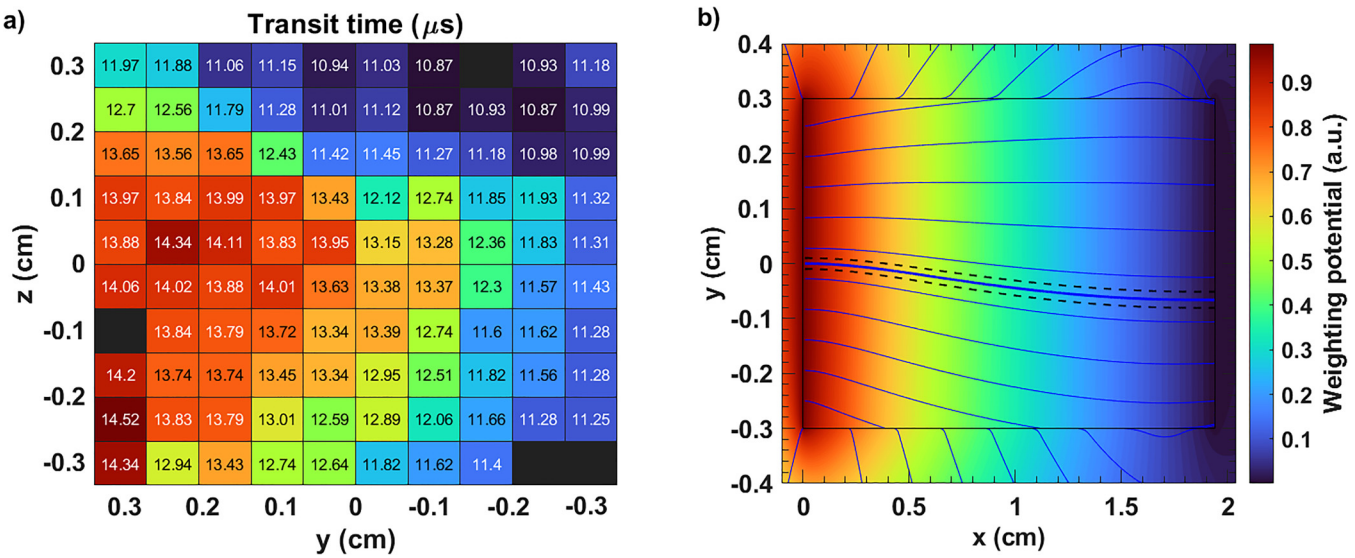

FIG. 7. (a) Transit time of steady-state electron current waveforms obtained at −600 V DC by scanning the front face. The transit time in the black regions was not discernable. (b) Modeled electric field in the horizontal cross section of the unpolarized bar detector and its surroundings. The region between the dashed lines encompasses the trajectories of all photogenerated carriers. The electric field lines are slightly shifted toward the negative *y* (and negative *z*) axis because of the asymmetric geometry of our setup (see Sec. IV).

affect the electron mobility at room temperature, where it is dominated by the optical phonon scattering. An impurity concentration of at least 10^{17} cm^{-3} would be necessary for this model.[29]

In addition, the bump formation may also be affected by the surface charge and its transport properties. Once the electrons and holes drifting through the detector reach the surface, they can no longer follow the field lines exiting the detector, see Fig. 7(b). They can only drift along the surface. The surface, therefore, experiences electron (hole) accumulation that appears even in the detector equipped with ohmic or blocking contacts. At the crossing point x = 1.7 cm [Fig. 7(b)], the nature of the surface current and charge changes: in between the cathode (x = 0 cm) and x = 1.7 cm, the surface current consists mainly of electrons, and the accumulated charge is negative. From x = 1.7 cm to the anode (x = 1.94 cm), it consists of holes. Surface charge forms this way and compensates the outward components of the electric field, which in the ideal case results in a uniform electric field similar to the planar sample. The inhomogeneity discussed above distorts the field lines, and therefore the surface charge compensates outward components of its electric field too. The lateral compensation, however, amplifies the longitudinal effect of the bulk inhomogeneity. However, this is not true for a conductive surface, which could drain the screening surface charge. Assuming the existence of the surface charge, the bump can also be explained by the variable surface conductivity analogous to the bulk case suggested above, although this model is disproved by the measurement with enlarged electrodes described in Sec. V B.

The remaining puzzle is the fact that we could detect the transit time despite the injecting anode. The low electric field strength near the anode would be expected to smear the waveform as was demonstrated in Ref. 21. According to our MC simulations, the calculated anode weighting field produces a more discernable transit time compared to the planar geometry (for a nonzero electric field beneath the anode). If the space-charge density in the region beneath the anode is lower than in the rest of the sample, the weighting field even produces the final increase in the CWF. The nearly flat profile of the DC electric field from the position 1.2 cm up to the anode, which is apparent in Fig. 5(b), is not consistent with the theory of space-charge limited current. This feature is probably caused either by a complex transport mechanism combining bulk and surface transport or more likely by the participation of electrons at the space-charge formation. A model that thoroughly investigates such features was presented in Ref. 30. As described above, the space-charge formation in bar detectors is complex. For further investigation, a 3D model of the electric field and electron (hole) position tracking is needed to distinguish between the surface and bulk charge contributions.

B. Modification of weighting fields

As was demonstrated in Sec. V A, the electric field beneath the anode is low in the unpolarized sample [red curve in Fig. 4(b)], and it is further lowered by the hole injection [Fig. 5(b)]. That is why we attempted to modify the geometry of the electrodes. We placed 20 × 30 mm^2 copper-foil electrodes at each end of the detector. These additional electrodes were connected to both the cathode and anode of the detector. Here, the foil and detector anode act as a single electrode. There were 6 × 6 mm^2 holes cut in the center of both foils (see Fig. 1) to allow for sample illumination. The electron CWFs measured in this geometry in an unpolarized and DC

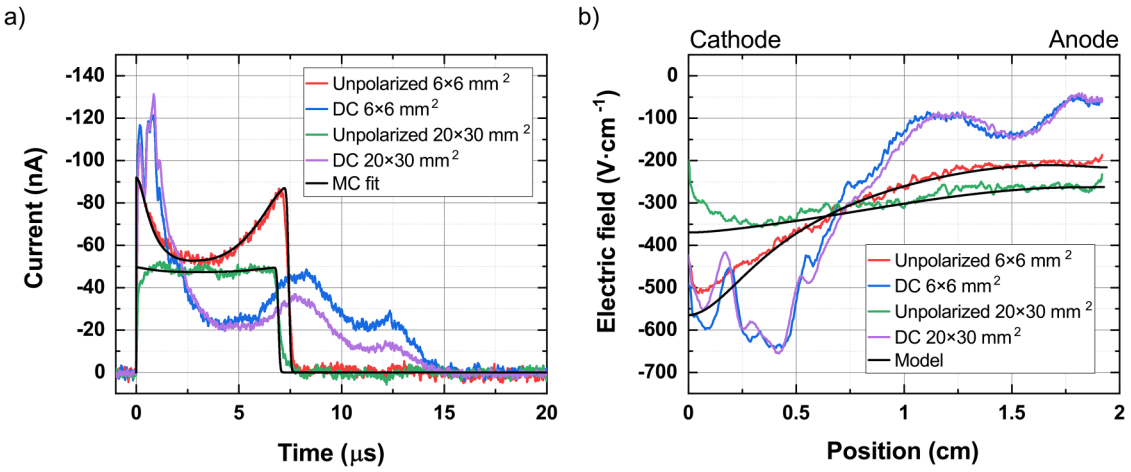

FIG. 8. (a) Comparison of electron current waveforms with and without additional 20 × 30 mm^2 electrodes in unpolarized and DC regimes at 600 V. (b) The electric field evaluated from the current waveforms in (a).

regime at −600 V are presented in Fig. 8(a) together with the CWFs measured without additional electrodes. The corresponding electric field is plotted in Fig. 8(b). As a result, both the CWF and electric field in the unpolarized regime are flatter than before. The ratio of the electric field beneath the cathode to the anode decreased from 2.6 to 1.4, and the transit time was reduced from 7.3 to 6.9 μs (6.6 μs in the planar detector with the same length). Surprisingly, the electric field in the steady state is almost the same as before. This finding further proves the model of hole injection and bulk inhomogeneity. The additional electrodes do not contribute to the bulk current (i.e., the injection ability of the anode and, therefore, the bulk space charge remains the same). Larger electrodes also play a similar role to the surface charge—they both lower the outward components of the electric field. The only difference is that the impact of larger electrodes is immediate, while the surface charge must form first. In both cases, the surface charge-formation stops when the electric field lines near the surface run parallel with it. In the end, the surface-charge density differs, but the resultant electric field is the same in both cases. The similarity of the DC electric fields with and without the additional electrodes indicates that surface charge indeed forms in the detector and plays a significant role in the detector performance. It also disproves the model of the CWF bump formation due to the variable surface conductivity. After the application of the enlarged electrodes, the surface current and related surface charge lowers, but the CWF bump is the same. The small difference between DC CWFs in Fig. 8(a) is caused purely by the weighting field of the collecting electrode (anode only vs anode plus additional collecting electrode).

The change of the detector geometry is clearly not enough to increase the electric field beneath the anode. For the polarization suppression and the restoration of the electric field, we propose the preparation of ohmic contacts. However, the manufacture of perfect ohmic contacts is difficult, especially for detectors with low electric fields, where even a small space-charge concentration significantly deforms the electric field. A more stable design could be reached by making slightly blocking contacts, which can be controlled by additional illumination as was demonstrated in Refs. 31 and 32. This would be especially useful for the fabrication of bar detector arrays, where each bar may have slightly different properties despite the use of standardized surface treatment and contact preparation methods. Array configuration of detectors will also lead to an improvement of the electric field uniformity in the array center (in the unpolarized regime). The situation near the edges of the array will remain the same; however, the preparation of non-conductive surfaces that allow surface charge formation would resolve this issue without the need for additional electrodes like those we tested here.

VI. CONCLUSIONS

We demonstrated the significance of L-TCT characterization of large-volume detectors. Monte Carlo simulations of current waveforms, together with modeled electric and weighting fields, revealed a remarkably high electron mobility-lifetime product $\mu_e\tau_e \geq 0.095\,\mathrm{cm^2\,V^{-1}}$ in the unpolarized detector. We found that in the steady state, the space-charge density linearly increases with applied bias. Further analysis revealed that a positive space charge up to $2.1 \times 10^9\,\mathrm{cm^{-3}}$ is formed at 1.8 kV due to hole injection, and its linear bias dependence is caused by the mutual dependence of the decreasing electric field strength beneath the anode and hole injection. In order to keep the electric field high in the whole detector, more reliable ohmic or slightly blocking contacts are required. The space-charge formation also caused an unusual bump in the central part of the electron current waveform. We explain this feature by the simultaneous negative and positive space-charge formation due to the spatial inhomogeneity of the detector. Experiments with enlarged electrodes show significant improvement of the electric field in the unpolarized detector. However, once the space charge is formed, the electric field is almost the

same as before. We consider this to be a proof of hole injection and surface-charge formation.

ACKNOWLEDGMENTS

This work was financially supported by the Grant Agency of the Czech Republic under No. P102-19/11920S, Grant Agency of Charles University under No. 393222, and Charles University under Grant No. SVV-2023-260720. R.B.J. acknowledges support from the U.S. Department of Energy, NNSA Office of Defense Nuclear Nonproliferation Research and Development and NNSA Minority Serving Institutions Partnership Program. R.B.J. also acknowledges support by Battelle Savannah River Alliance, LLC, under Contract No. 89303321CEM000080 with the U.S. Department of Energy. The publisher acknowledges the U.S. Government license to provide public access under the DOE Public Access Plan (http://energy.gov/downloads/doe-publicaccess-plan).

AUTHOR DECLARATIONS

Conflict of Interest

The authors have no conflicts to disclose.

Author Contributions

M. Betušiak: Conceptualization (equal); Data curation (equal); Formal analysis (equal); Investigation (equal); Visualization (equal); Writing – original draft (equal). **P. Praus:** Formal analysis (equal); Investigation (equal); Writing – review & editing (equal). **R. Grill:** Data curation (equal); Funding acquisition (lead); Writing – review & editing (equal). **E. Belas:** Formal analysis (equal); Resources (equal); Writing – review & editing (equal). **J. Pipek:** Software (lead); Writing – review & editing (equal). **A. E. Bolotnikov:** Formal analysis (equal); Writing – review & editing (equal). **R. B. James:** Formal analysis (equal); Writing – review & editing (equal).

DATA AVAILABILITY

The data that support the findings of this study are available from the corresponding author upon reasonable request.

REFERENCES

[1]A. E. Bolotnikov, K. Ackley, G. S. Camarda, C. Cherches, Y. Cui, G. De Geronimo, J. Fried, D. Hodges, A. Hossain, W. Lee, G. Mahler, M. Maritato, M. Petryk, U. Roy, C. Salwen, E. Vernon, G. Yang, and R. B. James, "An array of virtual Frisch-grid CdZnTe detectors and a front-end application-specific integrated circuit for large-area position-sensitive gamma-ray cameras," Rev. Sci. Instrum. **86**(7), 073114 (2015).

[2]Y. Kim and W. Lee, "Development of a Compton camera based on 3D position-sensitive virtual Frisch-grid CZT detectors," Nucl. Instrum. Methods Phys. Res. Sect. A **1053**, 168390 (2023).

[3]A. E. Bolotnikov, J. MacKenzie, E. Chen, F. J. Kumar, S. Taherion, G. Carini, G. De Geronimo, J. Fried, K. Kim, L. O. Girado, E. Vernon, and R. B. James, "Performance of 8×8×32 and 10×10×32 mm^3 CdZnTe position-sensitive virtual Frisch-grid detectors for high-energy gamma ray cameras," Nucl. Instrum. Methods Phys. Res. Sect. A **969**, 164005 (2020).

[4]P. Medina, C. Santos, and D. Villaume, in *Proceedings of the 21st IEEE Instrumentation and Measurement Technology Conference (IEEE Cat. No. 04CH37510)* (IEEE, 2004), Vol. 3, pp. 1828–1832.

[5]N. Goel, C. Domingo-Pardo, T. Habermann, F. Ameil, T. Engert, J. Gerl, I. Kojouharov, J. Maruhn, N. Pietralla, and H. Schaffner, "Characterisation of a symmetric AGATA detector using the γ-ray imaging scanning technique," Nucl. Instrum. Methods Phys. Res. Sect. A **700**, 10–21 (2013).

[6]A. Cola, I. Farella, N. Auricchio, and E. Caroli, "Investigation of the electric field distribution in x-ray detectors by Pockels effect," J. Opt. A: Pure Appl. Opt. **8**(7), S467–S472 (2006).

[7]M. Amman, J. S. Lee, P. N. Luke, H. Chen, S. A. Awadalla, R. Redden, and G. Bindley, "Evaluation of THM-grown CdZnTe material for large-volume gamma-Ray detector applications," IEEE Trans. Nucl. Sci. **56**(3), 795–799 (2009).

[8]H. Kim, L. Cirignano, A. Churilov, G. Ciampi, W. Higgins, F. Olschner, and K. Shah, "Developing larger TlBr detectors—Detector performance," IEEE Trans. Nucl. Sci. **56**(3), 819–823 (2009).

[9]K. Hitomi, O. Muroi, M. Matsumoto, T. Shoji, and Y. Hiratate, in *2000 IEEE Nuclear Science Symposium Conference Record (Cat. No. 00CH37149)* (IEEE, 2000), Vol. 1, pp. 4/127–4/130.

[10]Y. He, M. Petryk, Z. Liu, D. G. Chica, I. Hadar, C. Leak, W. Ke, I. Spanopoulos, W. Lin, D. Y. Chung, B. W. Wessels, Z. He, and M. G. Kanatzidis, "$CsPbBr_3$ perovskite detectors with 1.4% energy resolution for high-energy γ-rays," Nat. Photonics **15**(1), 36–42 (2021).

[11]J. Kunc, P. Praus, E. Belas, V. Dědič, J. Pekárek, and R. Grill, "Efficient charge collection in coplanar-grid radiation detectors," Phys. Rev. Appl. **9**(5), 054020 (2018).

[12]M. Bettelli, N. S. Amadè, D. Calestani, B. Garavelli, P. Pozzi, D. Macera, L. Zanotti, C. A. Gonano, M. C. Veale, and A. Zappettini, "A first principle method to simulate the spectral response of CdZnTe-based X- and gamma-ray detectors," Nucl. Instrum. Methods Phys. Res. Sect. A **960**, 163663 (2020).

[13]T. Takahashi and S. Watanabe, "Recent progress in CdTe and CdZnTe detectors," IEEE Trans. Nucl. Sci. **48**(4), 950–959 (2001).

[14]A. E. Bolotnikov, G. S. Camarda, E. Chen, S. Cheng, Y. Cui, R. Gul, R. Gallagher, V. Dedic, G. De Geronimo, L. Ocampo Giraldo, J. Fried, A. Hossain, J. M. MacKenzie, P. Sellin, S. Taherion, E. Vernon, G. Yang, U. El-hanany, and R. B. James, "CdZnTe position-sensitive drift detectors with thicknesses up to 5 cm," Appl. Phys. Lett. **108**(9), 093504 (2016).

[15]A. Mycielski, D. M. Kochanowska, A. Wardak, K. Gościński, M. Szot, W. Dobrowolski, G. Janusz, M. Górska, Ł. Janiak, W. Czarnacki, Ł. Świderski, J. Iwanowska-Hanke, and M. Moszyński, "Surface recombination and space-charge-limited photocurrent-voltage (PC-V) measurements in (Cd,Mn)Te samples—Kinetics of photocurrent (PC)," Sensors **22**(8), 2941 (2022).

[16]R. Matz and M. Weidner, "Charge collection efficiency and space charge formation in CdTe gamma and X-ray detectors," Nucl. Instrum. Methods Phys. Res. Sect. A **406**(2), 287–298 (1998).

[17]I. Vasylchenko, R. Grill, M. Betušiak, E. Belas, P. Praus, P. Moravec, and P. Höschl, "In and Al Schottky contacts comparison on P-type chlorine-doped CdTe," Sensors **21**(8), 2783 (2021).

[18]A. E. Bolotnikov, S. O. Babalola, G. S. Camarda, H. Chen, S. Awadalla, Y. Cui, S. U. Egarievwe, P. M. Fochuk, R. Hawrami, A. Hossain, J. R. James, I. J. Nakonechnyj, J. Mackenzie, G. Yang, C. Xu, and R. B. James, "Extended defects in CdZnTe radiation detectors," IEEE Trans. Nucl. Sci. **56**(4), 1775–1783 (2009).

[19]K. Suzuki, T. Sawada, and K. Imai, "Effect of DC bias field on the time-of-flight current waveforms of CdTe and CdZnTe detectors," IEEE Trans. Nucl. Sci. **58**(4), 1958–1963 (2011).

[20]E. Belas, R. Grill, J. Pipek, P. Praus, J. Bok, A. Musiienko, P. Moravec, O. Tolbanov, A. Tyazhev, and A. Zarubin, "Space charge formation in chromium compensated GaAs radiation detectors," J. Phys. D: Appl. Phys. **53**(47), 475102 (2020).

[21]J. Pipek, M. Betušiak, E. Belas, R. Grill, P. Praus, A. Musiienko, J. Pekarek, U. N. Roy, and R. B. James, "Charge transport and space-charge formation in $Cd_{(1-x)}Zn_{(x)}$ $Te_{(1-y)}Se_{(y)}$ radiation detectors," Phys. Rev. Appl. **15**(5), 054058 (2021).

[22]K. Suzuki, M. Shorohov, T. Sawada, and S. Seto, "Time-of-flight measurements on TlBr detectors," IEEE Trans. Nucl. Sci. **62**(2), 433–436 (2015).

[23]P. Praus, E. Belas, J. Bok, R. Grill, and J. Pekárek, "Laser induced transient current pulse shape formation in (CdZn)Te detectors," IEEE Trans. Nucl. Sci. **63**(1), 246–251 (2016).
[24]A. Musiienko, J. Pipek, P. Praus, M. Brynza, E. Belas, B. Dryzhakov, M.-H. Du, M. Ahmadi, and R. Grill, "Deciphering the effect of traps on electronic charge transport properties of methylammonium lead tribromide perovskite," Sci. Adv. **6**(37), eabb6393 (2020).
[25]Z. He, "Review of the Shockley–Ramo theorem and its application in semiconductor gamma-ray detectors," Nucl. Instrum. Methods Phys. Res. Sect. A **463**(1), 250–267 (2001).
[26]P. Guerra, D. G. Darambara, D. Visvikis, and A. Santos, in *2007 IEEE Nuclear Science Symposium Conference Record* (IEEE, 2007), pp. 2976–2979.
[27]H. Pernegger, S. Roe, P. Weilhammer, V. Eremin, H. Frais-Kölbl, E. Griesmayer, H. Kagan, S. Schnetzer, R. Stone, W. Trischuk, D. Twitchen, and A. Whitehead, "Charge-carrier properties in synthetic single-crystal diamond measured with the transient-current technique," J. Appl. Phys. **97**(7), 073704 (2005).
[28]S. M. Sze and K. K. Ng, *Physics of Semiconductor Devices* (John Wiley & Sons, Ltd, Hoboken, NJ, 2006), pp. 134–196.
[29]B. Segall, M. R. Lorenz, and R. E. Halsted, "Electrical properties of n-type CdTe," Phys. Rev. **129**(6), 2471–2481 (1963).
[30]K. Ridzonova, E. Belas, R. Grill, J. Pekarek, and P. Praus, "Space-charge-limited photocurrents and transient currents in CdZnTe radiation detectors," Phys. Rev. Appl. **13**(6), 064054 (2020).
[31]A. L. Washington, L. C. Teague, M. C. Duff, A. Burger, M. Groza, and V. Buliga, "Response of the internal electric field in CdZnTe to illumination at multiple optical powers," J. Electron. Mater. **41**(10), 2874–2879 (2012).
[32]J. Franc, V. Dědič, M. Rejhon, J. Zázvorka, P. Praus, J. Touš, and P. J. Sellin, "Control of electric field in CdZnTe radiation detectors by above-bandgap light," J. Appl. Phys. **117**(16), 165702 (2015).